

Microscopically constrained mean field models from chiral nuclear thermodynamics

Ermal Rrapaj^{1,2,*}, Alessandro Roggero^{2,†} and Jeremy W. Holt^{1,3}

¹*Department of Physics, University of Washington, Seattle, WA*

²*Institute for Nuclear Theory, University of Washington, Seattle, WA and*

³*Cyclotron Institute, Texas A&M University, College Station, TX*

We explore the use of mean field models to approximate microscopic nuclear equations of state derived from chiral effective field theory across the densities and temperatures relevant for simulating astrophysical phenomena such as core-collapse supernovae and binary neutron star mergers. We consider both relativistic mean field theory with scalar and vector meson exchange as well as energy density functionals based on Skyrme phenomenology and compare to thermodynamic equations of state derived from chiral two- and three-nucleon forces in many-body perturbation theory. Quantum Monte Carlo simulations of symmetric nuclear matter and pure neutron matter are used to determine the density regimes in which perturbation theory with chiral nuclear forces is valid. Within the theoretical uncertainties associated with the many-body methods, we find that select mean field models describe well microscopic nuclear thermodynamics. As an additional consistency requirement, we study as well the single-particle properties of nucleons in a hot/dense environment, which affect e.g., charged-current weak reactions in neutron-rich matter. The identified mean field models can be used across a larger range of densities and temperatures in astrophysical simulations than more computationally expensive microscopic models.

I. INTRODUCTION

Astrophysical phenomena such as core collapse supernovae and binary neutron star mergers, including the possible accompanying gravitational wave production and heavy-element nucleosynthesis in the matter outflow, are sensitive to the thermodynamics of isospin-asymmetric nuclear matter across many orders of magnitude in the nuclear density. In contrast to the hot ambient conditions characterizing these astrophysical environments, the structure and evolution of neutron stars are largely governed by the properties of cold and dense neutron-rich matter. Efforts are underway to combine astrophysical observations of neutron star properties [1–5], terrestrial laboratory experiments of finite nuclei and hot/compressed nuclear matter [6, 7], and microscopic many-body theory [8–13] to construct a more complete picture of the nuclear equation of state (EOS) across the range of conditions probed in supernovae and neutron star merger simulations.

Traditionally mean field models, based on either Skyrme phenomenology [14] or relativistic mean field (RMF) theory [15, 16], have been the method of choice for constructing nuclear equations of state for numerical astrophysics simulations. The energy scales probed are much below the regime where a perturbative treatment based on QCD, the fundamental theory of strong interactions, is feasible. Non-perturbative lattice QCD simulations may in principle overcome such difficulty, but at present multi-nucleon simulations are beyond the reach of modern supercomputers, although extracting a nucleon-nucleon interaction from lattice data is a topic

of intense current research (see e.g., [17–20]). An alternative is to construct a low-energy theory of strongly interacting matter, chiral effective field theory [21–24], which has already had many successes in the description of nuclear structure and reactions of light and medium-mass nuclei [25–35], as well as nucleonic matter at zero temperature [11, 36–44]. In recent years nuclear thermodynamics [45–49] from chiral effective field theory has been successful at describing the homogeneous phases of symmetric and asymmetric matter (including the equilibrium mixed liquid-gas phase) up to densities $\rho \simeq 2\rho_0$, where $\rho_0 = 0.16 \text{ fm}^{-3}$ is the saturation density of nuclear matter, and temperatures up to $T \simeq 25 \text{ MeV}$. However, the construction of an equation of state for direct use in astrophysical simulations is still in progress, since the description of nuclear matter at larger densities and temperatures is currently outside the scope of many-body perturbation theory with coarse-resolution chiral nuclear potentials. Here phenomenological mean field models can be used to extend the description, provided they match onto the low-energy theory.

In this work we analyze both Skyrme and RMF models for consistency with chiral nuclear thermodynamics. That is, we explore what conditions are required for mean field models [50–52] fit to the zero-temperature equation of state to be also consistent with the finite-temperature equation of state and transport properties of nuclear matter. In particular we will show that it is possible to find both (i) non-relativistic (i.e., Skyrme-type) as well as (ii) relativistic mean field models (RMF) that produce a thermodynamic equation of state for both pure neutron matter (PNM) and symmetric nuclear matter (SNM) compatible with many-body perturbation theory (MBPT) calculations employing chiral two- and three-nucleon interactions. Such models are also compatible with recent experimental constraints on nuclear matter properties [7], and their use in astrophysical simulations

* ermal@uw.edu

† roggero@uw.edu

may therefore serve as an accurate substitute for the more computationally demanding microscopic chiral equations of state.

The manuscript is organized as follows. In section II we compare MBPT calculations at both second- and third-order to non-perturbative quantum Monte Carlo calculations at zero temperature to assess uncertainties coming from neglected correlations in the perturbative treatment. This analysis is used in Section III to identify mean-field models for the zero-temperature equation of state compatible with results obtained from a coarse-resolution ($\Lambda = 414$ MeV) chiral interaction at next-to-next-to-next-to-leading order (N³LO) [53]. We then analyze the consistency of mean field models with chiral nuclear thermodynamics in section III B as well as nuclear single-particle properties in Section III C that affect charged-current weak reactions in proto-neutron stars. We end with a summary and conclusions.

II. AB INITIO UNCERTAINTY ESTIMATES ON MICROSCOPIC EOS MODELS

In the present section we analyze the theoretical uncertainties from many-body perturbation theory in computing the ground state energy of symmetric nuclear matter and neutron matter. As a nonperturbative benchmark we employ quantum Monte Carlo techniques. The goal is to identify the nuclear force models and density regimes where microscopic many-body calculations can impose the strictest constraints on phenomenological mean field models. One may already anticipate that interactions with low-momentum regulators would perform qualitatively better in this regard, especially in neutron matter, however our goal here is to have a quantitative understanding of these errors for a relevant set of potentials.

A. Method

The quantum Monte Carlo calculations presented here are based on the recently developed configuration interaction Monte Carlo (CIMC) method [11, 54, 55]. Projection QMC methods like CIMC are based on filtering out an eigenstate $|\Psi_0\rangle$ of the Hamiltonian H by repeated application of the propagator $\mathcal{P} = e^{-\Delta\tau(H-E_T)}$ on an initial state $|\Psi_1\rangle$:

$$|\Psi_0\rangle = \lim_{N_\tau \rightarrow \infty} \mathcal{P}^{N_\tau} |\Psi_1\rangle. \quad (1)$$

Here, N_τ is the number of imaginary time steps, E_T is an energy shift used to keep the norm of the wave function approximately constant, and $\Delta\tau$ is a finite step in ‘imaginary’ time: $\Delta\tau = i\Delta t$. The state $|\Psi_0\rangle$ is the eigenstate with the lowest eigenvalue within the subset of states having non-zero overlaps with $|\Psi_1\rangle$. The application of the propagator is carried out stochastically.

The main difference between the CIMC method and traditional continuum projection Monte Carlo methods is that in the CIMC method this stochastic projection is performed in Fock space (i.e., the basis is provided by the Slater determinants that can be constructed from a finite set of single particle (sp) basis states), as opposed to in coordinate space. As a result, non-local Hamiltonians do not pose any technical problems. In this work, we use the sp basis given by eigenstates of momentum and the z components of spin and isospin. A finite sp basis is chosen by imposing a ‘basis cutoff’ k_{\max} and convergence is checked by performing a sequence of calculations with increasingly larger values of the cutoff. This same sp basis is then employed to perform many-body perturbation theory calculations at both 2nd and 3rd order (see e.g., Ref. [56]).

In order for a stochastic sampling to be feasible, the matrix elements of the propagator, \mathcal{P} , need to be positive semi-definite. For nucleons interacting with realistic interactions this condition is never fulfilled due to the presence of repulsive contributions, giving rise to the so-called sign problem. In CIMC we circumvent this by using a coupled-cluster double (CCD) wavefunction to restrict the random walk in a subsector of the full many-body Hilbert space where the positivity of the propagator is guaranteed (for details see Appendix VI A and Ref. [55]). This introduces a systematic bias in the calculation (see Appendix VI A for an attempt to estimate its effects), but nevertheless the final energy eigenvalue E_0^{FN} is guaranteed to be an upper bound of the true ground state energy E_0 .

The formalism is fully compatible with the use of a three-body interaction in the hamiltonian (eg. in the same way as these are dealt with in CC-theory [43]), however in order to have more control on the fixed-node procedure the explicit inclusion of triplet correlations in the coupled cluster wavefunction has to be accounted for. Presently this poses strong limitations on the size of the sp basis that can be handled, making it difficult to reach convergence with respect to k_{\max} . An alternative approach based on cancellation techniques (see e.g., Ref. [57–59]), which may allow one to neglect explicit three-body correlations, is currently being explored.

B. Results

In this study of the convergence of MBPT we will use four different chiral NN interactions: the NNLO_{opt} from Ekström et al. [60], the two low-momentum cutoff interactions from Coraggio et al. [53] at N³LO with cutoffs of 414 MeV and 450 MeV and finally a version of the N³LO interaction with a 500 MeV cutoff from Entem and Machleidt [22, 24] where the N³LO contact terms have been refitted using the same regulator for all partial waves.

Calculations at constant density are performed by first choosing the number of particles in the system N and the target density ρ . The size L of the box is then given by

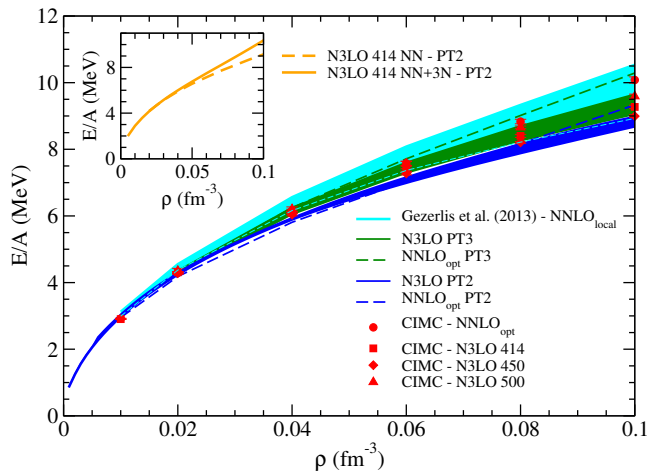


FIG. 1. (color online) Energy per particle of pure neutron matter as a function of density from different chiral interactions at NNLO and N³LO. Results at second-order (PT2) and third-order (PT3) in perturbation theory are shown together with those from configuration interaction Monte Carlo (CIMC) and auxiliary field diffusion Monte Carlo [39]. The inset shows the results at second-order in MBPT for the N³LO 414 interaction with and without three-nucleon forces.

$L = (N/\rho)^{1/3}$. In the present simulations the number of particles is fixed at the closed shell $N = 14$, and all of the results are converged with respect to the single-particle momentum cutoff k_{\max} , and we find that values of k_{\max} slightly higher than the cutoff Λ in the regulating function of the chiral potentials is needed for convergence (this is in good agreement with the findings in Ref. [11]). We have carefully examined the dependence on the system size and found that $N = 14$ provides reliable estimates at the low densities we are interested in, a more detailed discussion is provided in Appendix VIB. Furthermore, all the perturbative calculations are performed by including corrections to the nucleon self-energy at the Hartree-Fock level, in other words by performing normal ordering with respect to the Hartree-Fock state (for additional details see e.g., Ref. [56]). More detailed comparisons to results obtained using a free-particle spectrum can be found in Appendix VIC.

1. Pure Neutron Matter EOS

We first concentrate on the equation of state of pure neutron matter, shown in Fig. 1, for both perturbative methods and the nonperturbative CIMC method employing chiral two-body forces. The first qualitative observation that can be made is that the NNLO result lies consistently outside the N³LO band obtained by cutoff variation. However, as noted in Refs. [10, 61, 62] this variation may not be a reliable estimate of the spread in predictions at a given order in the chiral expansion. From the inset in Fig. 1 we observe that three-body interactions

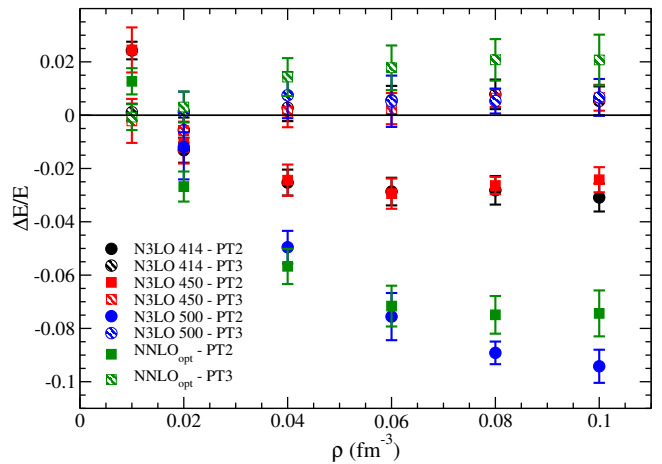


FIG. 2. (color online) Relative differences in energies obtained at different orders in perturbation theory with respect to the corresponding CIMC result for pure neutron matter. Notation same as in Fig. 1.

are needed for a quantitative study for densities $\rho \gtrsim 0.06 \text{ fm}^{-3}$. In the present section we focus on NN forces only, and consequently this is the highest density where we may draw rigorous conclusions.

Evaluating the convergence of the perturbative calculations in Fig. 1, we see that in PNM the third-order contributions are generally sufficient to bring the MBPT results very close to those from the non-perturbative CIMC, indicating a good convergence pattern for MBPT for all four interactions considered, regardless of the regularization cutoff. To estimate the errors corresponding to the perturbative convergence, we consider in Fig. 2 the relative difference between the CIMC results and the energies obtained at different orders in perturbation theory. We observe that the interactions split into two groups with N³LO 414 and 450 deviating from CIMC by $\approx 2 - 3\%$ at second order and the NNLO_{opt} and N³LO 500 interactions that have deviations of $6 - 8\%$. For all interactions the third-order calculations are compatible with CIMC for all densities apart from NNLO_{opt}, which at the highest densities has a small deviation of $\approx 1 - 2\%$.

One can study the effect of the bias coming from the fixed-node procedure by adding to the wavefunction a non-zero overlap with all states in the Hilbert space (triplet and higher order irreducible correlations) and checking the differences in the final estimate for the energy. In the case of PNM and for all four interactions this procedure gives results compatible with the energies obtained by employing the CCD wavefunction, which indicates that this source of systematic error is under control (a more detailed study of this systematic error is presented in Appendix VIA).

Before concluding this section we comment on the low density regime of neutron matter, which due to the large neutron-neutron scattering length ($a_{nn} \sim -19 \text{ fm}$) is very close to that of a non-perturbative unitary fermi gas.

From the results in Fig. 2 we may draw the (wrong) conclusion that at low densities ($\rho \lesssim 0.02 \text{ fm}^{-3}$) the perturbative calculations converge faster, with the second-order results at $\rho \approx 0.02 \text{ fm}^{-3}$ almost compatible with CIMC. This is however an artifact coming from the fact that the second-order predictions change from too attractive at high density to too repulsive at low ones, that is, the relative difference with CIMC changes sign at low densities (as is evident from Fig. 2). This is then in agreement with the expectation that at sufficiently low densities the convergence of MBPT breaks down.

2. Symmetric Nuclear Matter (SNM)

We now focus on the results for symmetric nuclear matter, shown in Fig. 3, that have been computed using $A = 28$ nucleons. In contrast to the neutron matter equation of state in the last section, here the various chiral two-nucleon forces give rise to larger variations. As a result the energy per particle from the NNLO interaction is now contained in the N^3LO band, which is mostly due to the N^3LO 500 results that are consistently less attractive than the rest for intermediate to high densities. Reaching low densities with this high-cutoff interaction is computationally more demanding, and since we already observed a lack of convergence in the simpler case of neutron matter, we will discuss in the following only the remaining three interactions. Another interesting feature apparent from the data (and compatible with earlier findings by Coraggio et al. [53]) is that at intermediate to high densities the third-order perturbative correction is negligible. To better understand this behavior we plot in Fig. 4 the ratio between third- and second-order perturbative corrections in both neutron and symmetric nuclear matter. We see that the third-order correction slowly changes sign around the empirical saturation density, giving an artificially small correction to the energy per particle.

If we were to evaluate the perturbativeness of the calculation by only comparing the magnitudes of the contributions at different orders in perturbation theory (see e.g., Fig. 4), we might draw the counterintuitive (and wrong) conclusion that the convergence pattern in SNM is much better than in PNM. That this is not the case can be understood by noticing that if the third-order calculation is already converged then the CCD wavefunction used in the fixed node procedure would be the exact ground state, but if that were the case then the third-order perturbative results and the ones predicted by CIMC should be on top of each other, which is not the case.

Another way to see this is to exploit the freedom in CIMC to tune the guiding wavefunction by truncating contributions beyond a given number of particle-hole excitations. The second-order energies contain information about 2p-2h excitations above the Hartree-Fock ground state, so any important effects coming from higher orders cannot be recovered in this low truncation of the

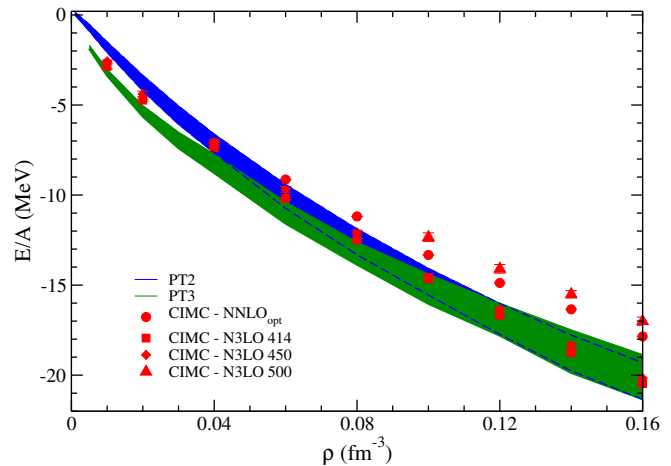


FIG. 3. (color online) Same as in Fig. 1, except for symmetric nuclear matter. The NNLO_{opt} results now are contained in the N^3LO bands.

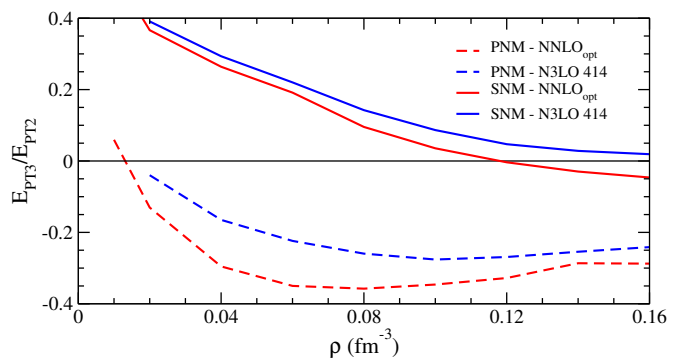


FIG. 4. (color online) Ratio of the third-order correction to the second-order one in PNM (dashed lines) and SNM (full lines) for NNLO_{opt} (red) and N^3LO 414 (blue).

MBPT expansion. We tested the NNLO_{opt} interaction at $\rho = 0.08 \text{ fm}^{-3}$ in both PNM and SNM and found that in the first case in order to recover the full CIMC results we have to allow up to 6p-6h contributions in the guiding wavefunction (with the 4p-4h truncation lying just outside the error bands) while for the latter case up to 12p-12h states are needed to reproduce the non-truncated CIMC result. Similar observations hold for the N^3LO 414 interaction that is used in subsequent sections of the paper, with 4h-4p being converged in PNM and 10p-10h for SNM. This observation is again in strong favor for enhanced non-perturbative features in the symmetric nuclear matter case, even for an interaction with a low-momentum cutoff.

We conclude that it may be misleading to evaluate the convergence of second-order calculations using only the magnitude of the next order as guidance (or equivalently using Padé extrapolations), especially in regimes where the third-order contributions are changing sign and are

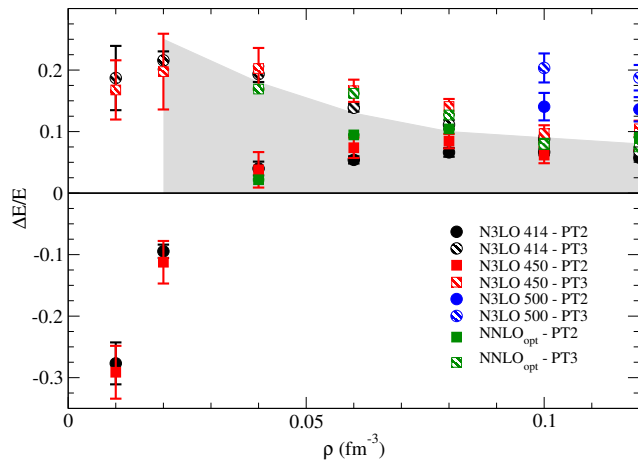


FIG. 5. (color online) Relative deviations of energies obtained at different orders in perturbation theory with respect to the corresponding CIMC result for symmetric nuclear matter. The gray band is a qualitative estimate of the uncertainties in the fixed-node approximation (see text for the details).

thus artificially small. Without the fourth-order results it is then difficult to judge convergence within MBPT itself and comparison with non-perturbative methods are important.

In Fig. 5 we plot the difference between the second- and third-order perturbative results for the symmetric matter equation of state and that obtained from CIMC. Recall that the main systematic error in the Monte Carlo calculations, the fixed-node error, is thought to be much more severe in this system especially at low densities due to the appearance of bound states that are extremely difficult to capture explicitly in the coupled-cluster ansatz for the guiding wavefunction. One of the appealing properties of the CIMC method however is that it is guaranteed to give an upper bound to the energy. As was mentioned above, by looking at the relative variations in Fig. 5 we can get the impression that second-order calculations provide as good (or better) estimates of the energy than those obtained at third order in the density range $0.04 - 0.10 \text{ fm}^{-3}$. This is a well known feature of asymptotic expansions (see e.g., Ref. [63]) like the one employed in MBPT (which does not involve any small parameter), where one finds in fact that the smallest error achievable (without employing resummations) is obtained by truncating the series at an optimal order N^* which may indeed be very small. However, given the present large uncertainties, no conclusive statement can be made.

A more rigorous statement can be made instead for lower densities $\rho < 0.04 \text{ fm}^{-3}$ by using the upper bound nature of CIMC energies: in the low density regime the errors introduced by stopping the perturbative expansion at second order are larger than $\approx 20\%$. One should be cautious about any statement on properties of nuclear matter in this regime, such as the spinodal instability region, coming from second-order MBPT. In order to

have more control in that region, comparisons to higher-order results are therefore needed before a better understanding of non-perturbative physics is achieved. In the intermediate-density regime, both second and third-order calculations of the ground state energy are very similar to each other and on average $7 - 10\%$ more bound than CIMC results. Due to the lack of control on the fixed-node errors, this would be the most reliable error band we can attribute to perturbation theory, but due to its qualitative nature it will not be used to discriminate among the various mean field models in subsequent sections. We note however that this estimate is consistent with the findings of Hagen et al. [43] in which the NNLO_{opt} interaction resulted in a difference between CCD and MBPT at second order of $\approx 12\%$ at $\rho = 0.06 \text{ fm}^{-3}$ to $\approx 8\%$ around saturation density.

III. EOS FROM MEAN FIELD MODELS

In the previous section we found that the two coarse-resolution chiral interactions at N³LO with cutoffs $\Lambda = 414$ and 450 MeV have good perturbative properties in PNM and SNM, with average errors on the order of $\Delta E/E \approx 2 - 3\%$ for the former and $\Delta E/E \approx 8 - 10\%$ for the latter in the vicinity of nuclear matter saturation density. In addition, as shown in fig. 1, for densities up to $0.05 - 0.06 \text{ fm}^{-3}$, the contribution to the energy per particle from 3N forces is negligible and the error estimates from our analysis can be used quantitatively to select mean field models that are consistent with second-order MBPT calculations at low densities. In the following we will adopt the most perturbative N³LO 414 interaction including both NN and 3N forces.

In astrophysical simulations of core-collapse supernovae and neutron star mergers, equations of state based on mean field models have been used for more than three decades. They provide a practical way of describing the physical properties of dense matter while being computationally inexpensive, thus allowing for the fast generation of data needed for simulations. Among these models those derived from Skyrme interactions are widely used for the description of both nuclei and infinite matter, with a prominent example being that of Lattimer and Swesty [14].

The general expression for the energy density functional of homogeneous matter is given by

$$\begin{aligned} \mathcal{E} = & \sum_{q=n,p} \frac{1}{2M_q} \tau_q + \frac{1}{4} t_0 \left[(2 + x_0) \rho^2 \right. \\ & \left. - (1 + 2x_0) \sum_{q=n,p} \rho_q^2 \right] + \frac{1}{8} \left[a \tau \rho + 2b \sum_{q=n,p} \rho_q \tau_q \right] \\ & + \frac{1}{24} t_3 \rho^\alpha \left[(2 + x_3) \rho^2 - (1 + 2x_3) \sum_{q=n,p} \rho_q^2 \right], \quad (2) \end{aligned}$$

where ρ is the density and τ is the kinetic energy density. Skyrme interactions represent a low-momentum ex-

pansion of an effective two-body NN interaction and are usually constrained by the properties of finite nuclei close to the valley of stability. The predictive power of Skyrme models however is difficult to assess away from the region in parameter space where it has been fitted. The astrophysical environments mentioned above span a wide range of densities, from a rarefied gas to dense matter possibly 2-5 times that of normal nuclei, and neutrons represent the vast majority of the nuclear composition. Moreover, these environments are characterized by high temperatures that can reach up to $T = 50$ MeV [64]. The reliability of effective Skyrme interactions to accurately cover this range of parameter space based on fits to terrestrial nuclei is an open question.

A first consistency check can be carried out using experimentally extracted constraints for nuclear matter properties. In Ref. [7] Dutra et al. have benchmarked a set of 240 Skyrme parametrizations against a set of 11 infinite matter constraints. Only 16 parametrizations were shown to meet all of these constraints. Due to the wide range of conditions encountered in supernovae simulations, a careful calibration of the models also in conditions that are difficult to achieve in terrestrial experiments is therefore important. Recent developments in both many-body techniques and nuclear forces allow the equation of state of PNM to be relatively well constrained at low densities. Using these results, together with properties of double-magic nuclei [65], Brown and Schwenk [50] have refitted from the consistent models in Ref. [7] a selected smaller set of six ‘‘best fit’’ Skyrme models: SKT1, SKT2, SKT3, SKa25s20, SKa35s20, Sv-sym32. In Ref. [50] two slightly different parameter sets for these interactions have been obtained by requiring a particular value for the effective mass ($m^*/m = 0.9$ or 1.0) in neutron matter at the density $\rho = 0.10$ fm $^{-3}$.

In this work we will consider all of these final 12 parametrizations. For mean field Skyrme models, theoretical uncertainties can be estimated through a careful extraction of the correlation matrix for the parameters entering the functionals [66–68]. In recent years important efforts have been devoted by the UNEDF collaboration to construct Skyrme parametrizations with reliable error quantifications; for this reason we have also considered the parametrizations UNEDF0 [69], UNEDF1 [70] and UNEDF2 [71]. For the other parametrizations there are no publicly available parameter correlations that can be used to study uncertainties and propagation of systematic errors. It is important to realize however that detailed error extrapolations in complicated simulations (like those for core-collapse supernovae) poses major technical challenges and therefore parametrizations whose central values are already close to the expected ones are to be preferred. In this work, we therefore focus on constraining mean field models from the low-density microscopic equation of state and study their properties at saturation density as described by Table I assuming negligible errors in the parameters. However, we would like to stress the need for a detailed study of

parametric uncertainties, which is outside the scope of this study. Such analysis would be greatly facilitated if new parametrizations would be published together with their parameter’s covariance matrix informations.

Recent astrophysical simulations also employ relativistic mean field models of the nuclear equation of state. The general expression for the energy density functional in terms of nucleon Ψ , scalar ϕ , vector V_μ , and vector isovector b_μ fields is given by

$$\begin{aligned} \mathcal{E} = & \sum_{s,t} \int \frac{d^3k}{(2\pi)^3} \sqrt{k^2 + (M_t - g_S\phi_0)^2} (f_{s,t} + \bar{f}_{s,t}) \\ & + \frac{1}{2} m_s^2 \phi_0^2 + \frac{\kappa}{3!} (g_S\phi_0)^3 + \frac{\lambda}{4!} (g_S\phi_0)^4 + \frac{\zeta}{8} (g_V V_0)^4 \\ & + \frac{1}{2} m_V^2 V_0^2 + \frac{1}{2} m_b^2 b_0^2 + 3\Lambda_V (g_V V_0)^2 (g_b b_0)^2. \end{aligned} \quad (3)$$

where, $(f_{s,t}, \bar{f}_{s,t})$ are the spin and isospin dependent fermi distribution functions for the nucleon and anti-nucleon respectively. And, (ϕ_0, b_0, V_0) are the ground state expectation values of the auxiliary fields. The expectation value ϕ_0 is obtained by solving

$$\begin{aligned} & \left(\frac{m_S}{g_S}\right)^2 (g_S\phi_0) + \frac{\kappa}{2} (g_S\phi_0)^2 + \frac{\lambda}{6} (g_S\phi_0)^3 \\ & = \sum_{s,t} \int \frac{d^3k}{(2\pi)^3} \frac{M_t - g_S\phi_0}{\sqrt{k^2 + (M_t - g_S\phi_0)^2}} (f_{s,t} + \bar{f}_{s,t}), \end{aligned} \quad (4)$$

and the vector ground state expectation values are obtained by solving a pair of coupled equations:

$$\begin{aligned} \rho_p + \rho_n &= \left(\frac{m_V}{g_V}\right)^2 (g_V V_0) + 2\Lambda_V (g_b b_0)^2 (g_V V_0) \\ &+ \frac{\zeta}{6} (g_V V_0)^3 \\ \rho_p - \rho_n &= \left(\frac{m_b}{g_b}\right)^2 (g_b b_0) + 2\Lambda_V (g_V V_0)^2 (g_b b_0). \end{aligned} \quad (5)$$

For a detailed description of the main features and how they match to supernovae and neutron star observations see Ref. [72]. The RMF models we focus on in this paper are the most commonly used in astrophysical calculations: FSUgold [73], IUFSU [74], TM1 [75], TMA [76], DD2 [77], SFHx [78], SFHo [78]. Similar to the work on Skyrme models, in Ref. [79] a full analysis of 263 different RMF parametrizations have been carried out with the same set of 11 infinite matter constraints, and only the Z271v5 and Z271v6 [80] parametrizations were found to meet the criteria. Hence, we also include them in our analysis.

A. Zero Temperature

As the purpose of this work is to gradually select among the many available mean field models those that can be used to understand the thermodynamic evolution of a binary merger or core collapse supernova and are consistent with our current knowledge of baryonic matter, we proceed as follows:

In figures 6 and 7 we select among relativistic and skyrme models respectively based on our findings from previous sections by comparing to the chiral N^3LO 414 interaction with NN and 3NF forces. We have compared our constraints with [50] and have found that our values are well within the bands in that work. For the remaining models, we employ constraints from Dutra et al. [7], and since the refitted Skyrme parametrizations selected in Ref. [50] are essentially new parametrizations, they need to be tested for validity.

We observe in Fig. 6 that phenomenological models have wide variations, even down to very low densities, in contrast to the microscopic predictions shown in Fig. 1. This model dependence can be traced to the weak correlation between the low-density neutron matter equation of state and the observables used to constrain the phenomenological models. Among the relativistic models only Z271v6 agrees with the uncertainty bands from microscopic calculations and therefore is the only parametrization considered any further in this analysis. We notice however that both the DD2 and SFHx parametrizations are very close to fulfilling the low-density constraints, and therefore we will test them against the set of constraints from Dutra et al. [7] in the following. For the non-relativistic models all the UNEDF parametrizations fail the low density constraints. We note however that it should be possible to include low density neutron matter calculations as done in Ref. [50] to achieve a better agreement. Although the low-density regime is not important for some neutron star properties, for instance the mass-radius relation, it is essential for analyzing electron neutrino transport during core-collapse supernovae.

In Fig. 7 we show the chiral equation of state and low-density uncertainty estimates together with the various Skyrme models that satisfy also the infinite matter constraints. The uncertainty band for neutron matter at $\rho = 0.02 \text{ fm}^{-3}$ excludes parametrizations SKT1-1.0, SKT2-1.0, SKT3-1.0, Ska35s20-1.0, Sv-sym32-1.0. However, the Ska35s20-1.0 Skyrme interaction just misses the low-density constraint, and we choose to consider it in further analyses as the best representative of the models with $m^*/m = 1.0$.

In the high-density regime the differences between mean field models and the chiral equation of state increase. For instance, at saturation density the variations in Skyrme parametrizations are between 5% and 10% more repulsive than the perturbative prediction, while

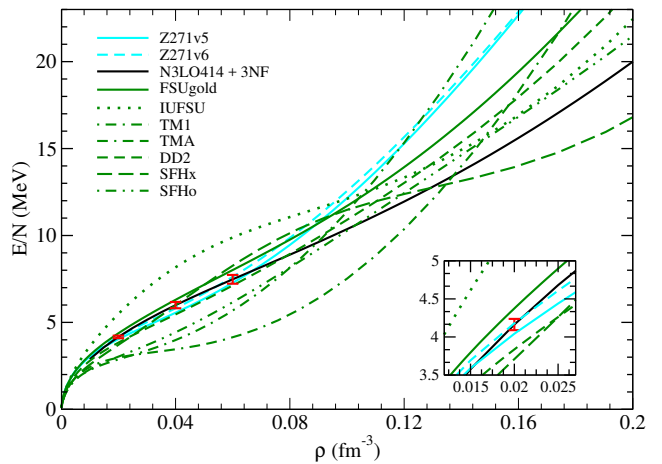


FIG. 6. (color online) Energy per particle for neutron matter at $T = 0$, where the red bars show the constraints derived in the previous sections. In the inset we show a close-up of the low-density ($\rho \simeq 0.02 \text{ fm}^{-3}$) regime.

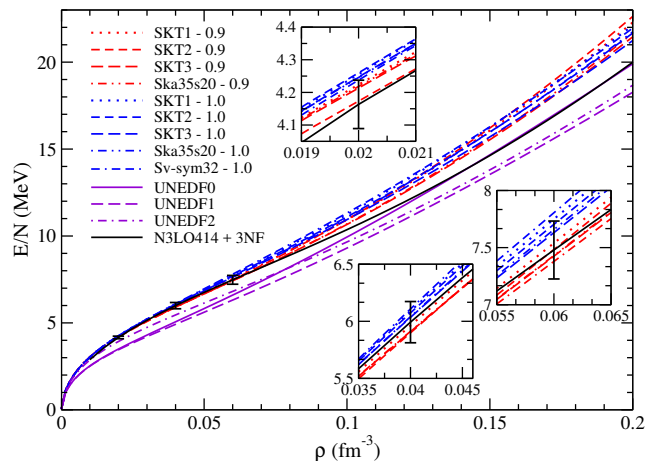


FIG. 7. (color online) Equation of state for pure neutron matter. The insets show the uncertainty bands from neglected correlations in the perturbative treatment from Section II.

RMF models can differ by up to 40%. At these densities and beyond, theoretical error bands on the perturbative calculation increase due to the approximate treatment of three-body forces in the two-body normal-ordering approximation [81–84] at second-order in perturbation theory, whose uncertainties have not been evaluated in the present work (but see Ref. [85] for an initial study). We therefore do not place strong constraints on the mean field models from chiral effective field theory beyond low densities. We note however that given the results obtained at low densities a 5% error is to be expected and we can therefore assume that the parametrizations SKT1-0.9, SKT2-0.9, SKT3-0.9, Ska35s20-0.9 and Ska35s20-1.0 are in very good agreement with the results obtained from chiral interactions.

For the symmetric nuclear matter equations of state shown in Fig. 8 the predictions of different models are

Name	compatible	K_m (MeV)	K' (MeV)	J (MeV)	L (MeV)	$K_{\tau,v}$ (MeV)	$S(\rho/2)/J$	$3P_{PNM}/L\rho_0$
Ska25s20 - 0.9	-	220	413	32.1	50.9	-345	0.66	1.0
Ska35s20 - 0.9	+	240	378	32.2	53.6	-374	0.65	1.0
SKT1 - 0.9	+	238	382	32.6	55.3	-378	0.65	1.0
SKT2 - 0.9	+	240	385	33.1	58.0	-385	0.64	1.0
SKT3 - 0.9	+	237	382	32.0	52.6	-370	0.65	1.0
Sv-sym32 - 0.9	-	234	384	31.5	49.5	-360	0.66	1.0
Ska25s20 - 1.0	-	220	415	32.0	46.4	-355	0.67	1.0
Ska35s20 - 1.0	+	240	379	32.2	50.6	-385	0.66	1.0
SKT1 - 1.0	+	237	384	32.5	51.5	-386	0.66	1.0
SKT2 - 1.0	+	236	387	32.3	50.4	-381	0.66	1.0
SKT3 - 1.0	+	237	385	33.0	48.9	-377	0.66	1.0
Sv-sym32 - 1.0	+	237	375	32.0	47.7	-387	0.66	1.1
DD2	-	243	-169	31.7	55.0	-461.7	0.66	1.0
SFHx	-	239	457	28.7	23.2	-	-	1.0
Z271v5	+	270	734	34.0	73.9	-389	0.57	1.0
Z271v6	+	270	734	33.8	70.9	-388	0.57	1.0
N3LO414 + 3NF	+	223	270	32.5	53.8	-424	0.70	1.0
Range of constraint		190-270	200-1200	30-35	40-76	-760 to -372	0.57-0.86	0.9-1.1

TABLE I. Constraints on the properties of infinite nuclear matter from Dutra et al. [7, 79]. See text for definitions and details.

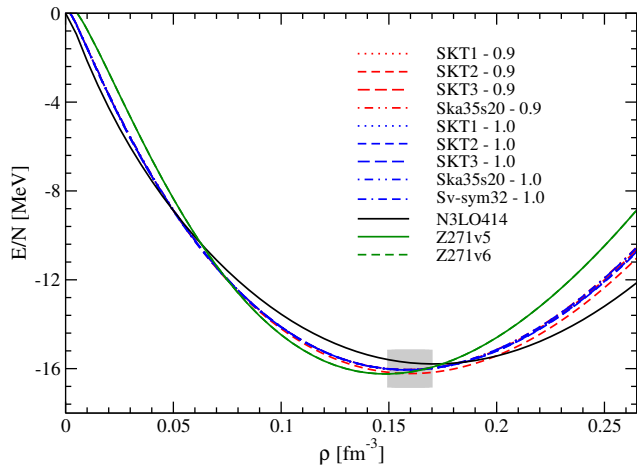


FIG. 8. (color online) Same as Fig. 7 but for symmetric nuclear matter. We allow a 5% tolerance at nuclear matter saturation density shown by the grey box.

very similar, reflecting the fact that the parametrizations have been predominantly fitted to properties of infinite matter around and below the saturation density. As discussed in Section II, in this case we do not have a tight constraint on the perturbation theory uncertainties, and considering an average error of $\Delta E/E \approx 10\%$, all parametrizations in Fig. 8 are compatible with the perturbative results. As a further check we compare the predictions for the saturation point and find that all parametrizations are able to reproduce the empirical result within the 5% box shown in Fig. 8. We therefore cannot use the $T = 0$ SNM equation of state to further

eliminate mean field models.

In Table I we summarize the numerical infinite matter constraints from Ref. [7]. In particular, the observables listed are the symmetric matter incompressibility

$$K_m = 9 \left. \frac{\partial P}{\partial \rho} \right|_{\rho_0} \quad (6)$$

at saturation density, where $P = \rho^2 \frac{\partial(E/N)}{\partial \rho}$ is the pressure; the derivative of the incompressibility with respect to density (the so-called skewness parameter)

$$K' = -27\rho_0^3 \left. \frac{\partial^3(E/N)}{\partial \rho^3} \right|_{\rho_0}; \quad (7)$$

the symmetry energy

$$J = S(\rho_0) = \left. \frac{\partial(E/N)}{\partial \delta_{np}^2} \right|_{\rho_0}, \quad (8)$$

where $\delta_{np} = \frac{\rho_n - \rho_p}{\rho_n + \rho_p}$ is the isospin asymmetry; the symmetry energy slope

$$L = 3\rho_0 \left. \frac{\partial S}{\partial \rho} \right|_{\rho_0}; \quad (9)$$

the isospin incompressibility

$$K_{\tau,v} = K_{\text{sym}} - L \left(6 + \frac{K'}{K_m} \right), \quad (10)$$

where $K_{\text{sym}} = 9\rho_0^2 \left. \frac{\partial^2 S}{\partial \rho^2} \right|_{\rho_0}$; the ratio between the symmetry energy at half saturation density and its value at ρ_0 ; and finally the quantity $3P_{\text{PNM}}/L\rho_0$, where P_{PNM} is the pressure in PNM at saturation density. In addition, there are four ‘‘band constraints’’ on the symmetric nuclear matter and pure neutron matter equations of state in specific density regimes below and above nuclear saturation:

1. P_{SNM} for $1.2 < \frac{\rho}{\rho_0} < 2.2$
2. P_{SNM} for $2 < \frac{\rho}{\rho_0} < 4.6$
3. P_{PNM} for $2 < \frac{\rho}{\rho_0} < 4.6$
4. $(E/N)_{\text{PNM}}$ for $0.014 < \frac{\rho}{\rho_0} < 0.106$.

First we note that the two RMF parametrizations that were close to reproduce low-density neutron matter constraints, DD2 and SFHx, do not satisfy the constraints. In particular DD2 has a skewness parameter K' with the wrong sign ($K' = -168.7 \text{ MeV}$) while SFHx has too low a value for the slope L of the symmetry energy ($L = 23.18 \text{ MeV}$). Furthermore, as can be seen from Table I, some of the new parametrizations are inconsistent with the empirical constraints in Ref. [7]. Specifically, Ska25s20-0.9, Ska25s20-1.0 and Sv-sym32-0.9 fail to meet the constraint for isospin incompressibility.

We note that the discrepancies between our results for the symmetry energy and the ones reported in Table I from Ref. [50] are due to different definitions. In our case we follow Ref. [7] and start with the generic expression at arbitrary isospin asymmetry $\delta_{np} = \frac{\rho_n - \rho_p}{\rho} = 1 - 2y_p$ and define S as the second derivative of the energy per particle with respect to y_p , as shown previously, while in Ref. [50] S is obtained as the difference between the PNM and the SNM equations of state at a given density. For microscopic approaches (like MBPT) these two definitions of S give very similar values (see e.g., [86, 87]).

As mentioned above the chiral 414 MeV interaction is used at second order in many-body perturbation theory with two- and three-body forces. Results using the potential with a cutoff of 450 MeV are very close to those from the N³LO 414 potential. We see that in all cases the microscopic calculations of the equation of state with this potential are consistent with the empirical infinite matter constraints considered in Ref. [7]. We note that all models considered meet the band constraints.

B. Finite Temperature

In this section we focus on the nuclear thermodynamic equation of state of homogeneous matter from the mean field models that were found in the last section to be compatible with the zero-temperature equation of state from low-momentum chiral nuclear forces and analyze the conditions necessary for consistency at finite temperature. We therefore focus on only the parametrizations

SKT1-0.9, SKT2-0.9, SKT3-0.9, Ska35s20-1.0, Ska35s20-0.9 and Z271v6. Since there are no nonperturbative microscopic calculations available, we cannot assign uncertainty bands at specific densities as in the zero-temperature analysis. However, one would not expect the many-body perturbation expansion to change dramatically by including finite-temperature effects, and therefore we use the chiral interaction N3LO414 together with 3NF forces to be a qualitative guiding tool for low-density thermodynamical properties. The aim is to identify mean field models that quantitatively reproduce chiral nuclear thermodynamics at low to moderate densities and temperatures. The coefficients for the refitted Skyrme parametrizations that meet our selection criteria so far are given in Table II.

The mean field models we are considering are fitted to nuclei and infinite matter at $T = 0$ and contain no empirical input at finite temperature. The nucleon effective mass however controls the density of states and therefore aspects of thermal excitations. We anticipate that the single-particle properties of nucleons in mean field models will control whether the associated thermodynamic equations of state will be consistent with those from perturbative chiral interactions. We choose low- and high-temperature representative values $T = 5, 25 \text{ MeV}$.

The formalism employed in this section is self-consistent Hartree-Fock theory which treats the density matrix as effectively of one-body type. The problem of treating interactions properly is cast into an energy density functional for which a corresponding local density is found by minimization of the energy. The Skyrme and RMF models fall into this category. In the thermodynamic limit an ensemble equivalence is guaranteed, and the canonical or grand-canonical potential can be minimized. As we opt to have temperature T and density ρ as external fixed parameters, we work in the canonical ensemble. The set of self-consistent equations to be satisfied at Hartree-Fock level is given by Eqs. (11) and (12) below. For a given momentum-dependent nucleon single-particle spectrum $\epsilon_{s,t}(k)$, where s and t are the spin and isospin quantum numbers, the energy density and entropy density can be calculated from

$$f_{s,t}(k) = \left[1 + e^{(\epsilon_{s,t}(k) - \mu)/T} \right]^{-1}, \quad (11)$$

$$\rho = \sum_{s,t} \int \frac{d^3k}{(2\pi)^3} f_{s,t}(k),$$

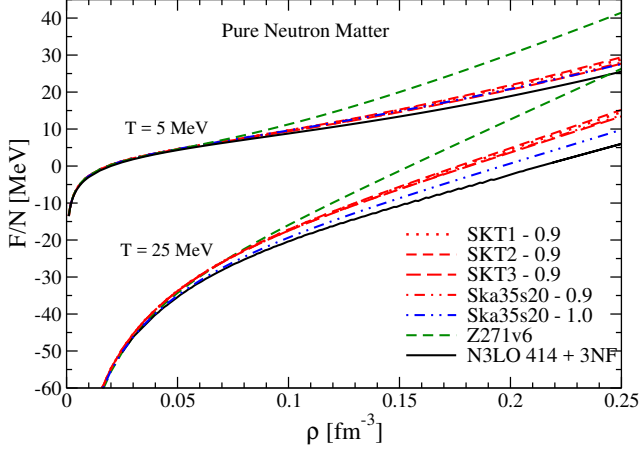
$$\tau = \sum_{s,t} \int \frac{d^3k}{(2\pi)^3} k^2 f_{s,t}(k),$$

$$S/V = - \sum_{s,t} \int \frac{d^3k}{(2\pi)^3} [f_{s,t} \ln f_{s,t} + (1 - f_{s,t}) \ln(1 - f_{s,t})],$$

where a sum over all discrete quantum numbers is performed (spin and isospin). The chemical potential can be found by inverting the expression for the density. From

Name	α	\mathbf{a} (MeV fm ⁵)	\mathbf{b} (MeV fm ⁵)	\mathbf{t}_0 (MeV fm ³)	\mathbf{x}_0	\mathbf{t}_3 (MeV fm ^{3(1+\alpha)})	\mathbf{x}_3
Ska35-0.9	0.35	-172.485	172.087	-1767.71	0.282732	12899.2	0.413266
SKT1-0.9	1/3	-112.324	142.467	-1810.72	0.28223	12863.0	0.392585
SKT2-0.9	1/3	-113.857	143.999	-1807.87	0.267778	12802.4	0.366144
SKT3-0.9	1/3	-124.432	148.492	-1812.16	0.288584	12906.6	0.416129
Ska35-1.0	0.35	-2.41114	-0.507978	-1767.92	0.247025	12910.2	0.220377

TABLE II. Parameters for the refitted Skyrme interactions of Ref. [50].

FIG. 9. (color online) Free energy per nucleon in pure neutron matter at temperatures $T = 5, 25$ MeV for the 414 MeV chiral nuclear potential and mean field models.

the energy density functional, an effective mass and mean field shift can be extracted:

$$M_t^* = \frac{1}{2} \left(\frac{\delta \mathcal{E}}{\delta \tau_t} \right)^{-1} \quad (12)$$

$$U_t = \frac{\delta \mathcal{E}}{\delta \rho_t},$$

which gives a single-particle spectrum of the form

$$\epsilon_t(k) = k^2/2M_t^* + U_t. \quad (13)$$

In Figs. 9 and 10 we plot the free energy per particle of neutron matter and isospin-symmetric nuclear matter for the microscopic and mean field models under consideration. We employ the Matsubara finite-temperature formalism up to second order in perturbation theory to compute the free energy per particle from the chiral two- and three-body potentials. Additional details can be found in Refs. [48, 49]. At $T = 5$ MeV the PNM free energy is similar to that at zero temperature, where the mean field equations of state are consistently less attractive than that from chiral low-momentum interactions. However, at $T = 25$ MeV the Skyrme mean field models exhibit larger variations in the free energy. In particular smaller values of the effective mass result in a larger kinetic energy contribution and a small entropy term, both

of which reduce the attraction at high temperatures. In symmetric nuclear matter at low temperatures there is consistency between all mean field models considered and the chiral equation of state. At the largest temperature considered ($T = 25$ MeV) the Skyrme models remain in good agreement with each other, owing to the very similar values of the effective masses, but deviate by about 5 MeV from the chiral effective field theory prediction. This pattern is different than that in the neutron matter equation of state, and it suggests that the average effective nucleon mass in symmetric nuclear matter is smaller than that in the Skyrme mean field models.

To explain the difference more carefully, we study the single-particle spectrum. The relativistic and nonrelativistic models treat this quantity (as well as the chemical potential) differently. We first compare the non-relativistic reduction of the single-particle spectrum in RMF models to that in the Skyrme models:

$$e_{t\text{Skyrme}}(k) = \epsilon_t(k) - \mu_t = \frac{k^2}{2M_t^*} + U_t - \mu_t^{\text{NR}}$$

$$\equiv \frac{k^2}{2M_t^*} + U_t^*,$$

$$e_{t\text{RMF}}(k) = \epsilon_t(k) - \mu_t = \sqrt{k^2 + M_t^{*2}} + U_t - \mu_t^{\text{R}} \quad (14)$$

$$\approx \frac{k^2}{2M_t^*} + M_t^* + U_t - \mu_t^{\text{R}}$$

$$\equiv \frac{k^2}{2M_t^*} + U_t^*.$$

At the HF level the low-energy spectrum can be accurately modeled by an effective mass and mean field shift, both density dependent. We show in Figs. 11 and 12 the effective mass and mean field shifts in neutron matter and symmetric nuclear matter for the models under consideration. In the case of SNM, the lower value of the effective mass corresponds to a higher value of the energy per baryon for Skyrme interactions, which results from a larger kinetic energy contribution to the free energy. Since the mean field shifts for the different Skyrme interactions with $M^*/M = 0.9$ in PNM at $\rho = 0.1$ fm⁻³ are nearly identical, the kinetic contribution dominates the difference while the interaction contribution depends mostly on the density.

In contrast, RMF models predict smaller effective masses and larger (negative) effective mean field shifts.

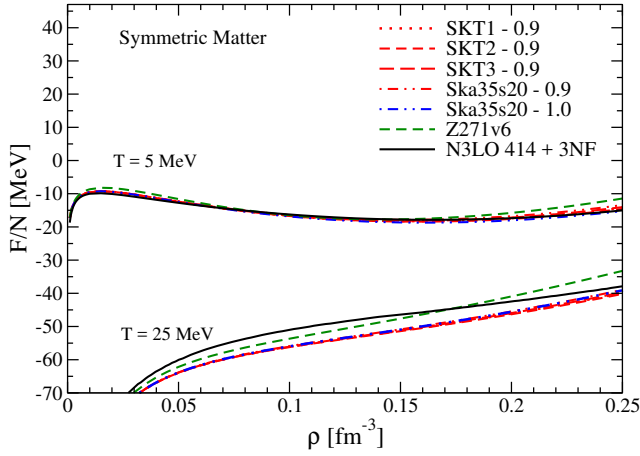


FIG. 10. (color online) Same as Fig. 9 except for symmetric nuclear matter.

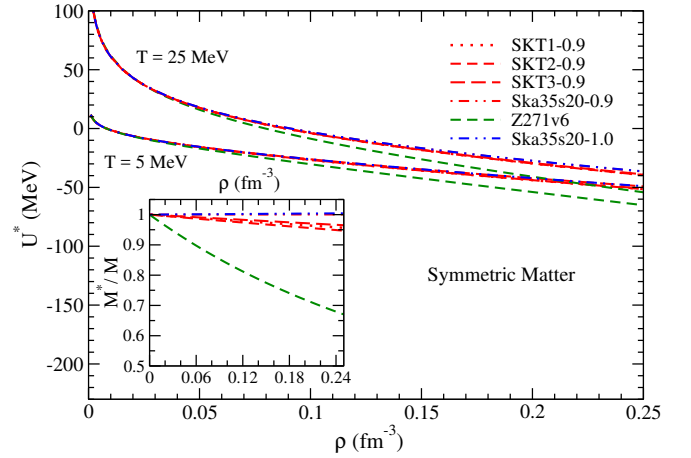


FIG. 12. (color online) Same as in Fig. 11 except for symmetric nuclear matter.

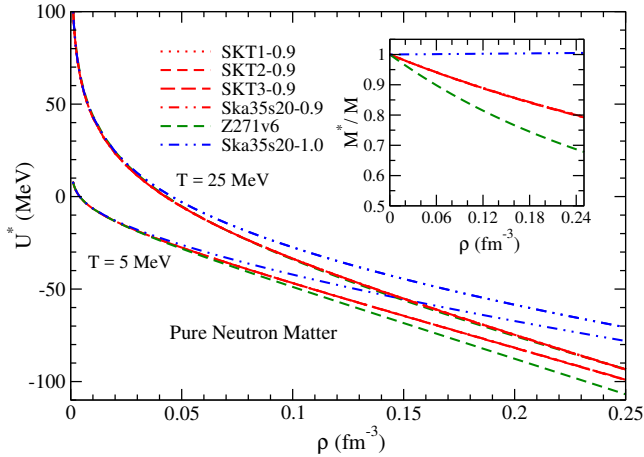


FIG. 11. (color online) Neutron mean field shift and effective mass in pure neutron matter. Note that all “Sk...0.9” Skyrme interactions have nearly identical effective masses.

In the case of Z271v6 these effects balance in SNM, with the effective mass becoming more important only at higher densities (higher values of F/N). However, for PNM, Z271v6 has a very small effective mass which leads the kinetic energy to dominate over interactions as can be seen by higher values of F/N for the whole density range depicted in fig. 9. Despite the effective mass and energy shifts being very different between these two models, the free energies predicted are relatively similar. To understand the physical relevance of these two parameters, we have to study physical ‘observables’ which are specifically susceptible to them. In the next section we focus on neutrino response and thermodynamic evolution, both sensitive to the single-particle spectrum, to differentiate Skyrme and RMF models.

C. Effect of Single-Particle Properties

Nuclear thermodynamics is governed by the free energy per nucleon as a function of the density and temperature. Related quantities such as pressure, entropy and chemical potential are given in terms of the free energy through standard thermodynamic relations. Dynamical phenomena in nuclear matter at finite temperature are strongly related to the single-particle properties of nucleons, and as shown in the last section the effective mass and mean field shift can be quite different between two models that nevertheless have similar equations of state. Thus, to explore a different set of consistency requirements between mean field models and microscopic nuclear dynamics we employ an analysis of the neutrino response and isentropic curves for core-collapse supernovae. We focus on Ska35s20-0.9, Ska35s20-1.0, and Z271v6, which are the “best fit” parametrizations from nonrelativistic and relativistic mean field models to chiral equations of state at finite temperature.

1. Neutrino Response

Charged-current weak reactions are primarily responsible for setting the electron neutrino opacity in the warm ($T = 5 - 8$ MeV) and dilute ($\rho = 0.001 - 0.01\rho_0$) region of last scattering (the neutrinosphere) for neutrinos diffusing from the core of a newly born proto-neutron star [88–90]. Owing to the nondegenerate conditions, the fermi distribution functions for neutrons and protons are strongly smeared in the vicinity of the chemical potential. The proton and neutron energy shifts are primarily responsible for modifications to neutrino and anti-neutrino mean free paths, but the momentum dependence of the single-particle potential can also be relevant for low-density moderate-temperature conditions. The inverse mean free path of ν_e from the reaction $\nu_e + n \rightarrow e^- + p$

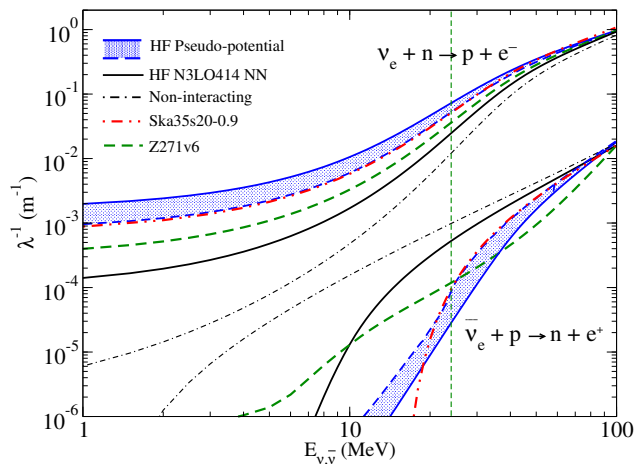


FIG. 13. (color online) Charged-current rates at β equilibrium: $T = 8$ MeV, $\rho = 0.02$ fm $^{-3}$. The vertical dashed line indicates the ‘thermal’ energy, $E_{\nu_e, \bar{\nu}_e} = 3T$.

follows from Fermi’s golden rule and is given by

$$\lambda_{\nu_e}^{-1} = \frac{2}{(2\pi)^5} \int d^3 p_n d^3 p_e d^3 p_p \mathcal{W}_{fi} \quad (15)$$

$$\times \delta^{(4)}(p_{\nu_e} + p_n - p_e - p_p) f_n (1 - f_e) (1 - f_p),$$

where f is the fermi distribution function and \mathcal{W}_{fi} is the transition probability. Both depend on the single-particle spectrum, and due to the energy-momentum conserving delta function, the phase space is also highly impacted by M^* and U^* .

We consider β -equilibrated matter at the density $\rho = 0.02$ fm $^{-3}$ and temperature $T = 8$ MeV. We show in Table III the proton and neutron effective masses and energy shifts for the mean field models considered as well as for the chiral n3lo414 potential at Hartree-Fock level and the pseudo-potential which resums iterated ladder diagrams (without Pauli blocking) to all orders in perturbation theory and which is defined in terms of nucleon-nucleon scattering phase shifts (see Ref. [91] for additional details). The effective mass and mean field shift for the chiral interactions come from a global fit of the single-particle spectrum from $k = 0$ to $k = 2k_f$. Note that for the temperature and density considered here, the two Skyrme parametrizations Ska35s20-0.9 and Ska35s20-1.0 give nearly identical single-particle properties.

Given the paramount importance of charged-current absorption rates in determining the decoupling regions, and thus the energy spectra of ν_e and $\bar{\nu}_e$, we plot in Fig. 13 the opacity from two mean field equations of state. We observe that for electron neutrino absorption all mean field models are consistent with the lower bound provided by the chiral Hartree-Fock approximation and the upper bound set by the pseudo-potential. The Skyrme Ska35s20-0.9 mean field prediction is in good agreement with the pseudo-potential results, given that both models predict large values of $\Delta U = U_n - U_p$. Since the chiral EFT calculation is only at the self-

Model	Y_p	M_n^*/M_n	M_p^*/M_p	$-U_n$	$-U_p$	ΔU
HF Pseudo-potential	4.9%	0.65	0.42	22	55	33
HF Pseudo-potential (mod)	3.8%	0.78	0.57	18	42	23
HF N3LO414	2.2%	0.95	0.89	8	16	8
RMF: Z271v6	2.8%	0.96	0.96	9	22	13
Skyrme: Ska35s20-0.9	3.3%	0.98	1.0	9	26	17

TABLE III. The Hartree-Fock (HF) effective masses M^* and energy shifts U (in units of MeV) for protons and neutrons in beta equilibrium at $n_B = 0.02$ fm $^{-3}$ and temperature $T = 8$ MeV. The difference in proton and neutron mean-field shifts is given by $\Delta U = U_n - U_p$, and the proton fraction is denoted by Y_p .

consistent Hartree-Fock level, considerable attraction in the iterated tensor force channel is missing, and results much closer to those from the pseudo-potential are expected when second-order perturbative contributions are included. We plan to study these effects more carefully in future work. To completely determine the neutrino opacity, neutral current reactions are needed. Particularly for the case of $\bar{\nu}_e$ in the lower regions of the power spectrum, brehmsstrahlung absorption rates dominate [91–93].

2. Supernova Isentropic Curves

During the core collapse of a massive star, the entropy per baryon changes from about $1 k_B$ to $2\text{--}3 k_B$, and the adiabatic (isentropic) approximation can be used to describe the thermodynamic evolution during such a short time scale. The temperature versus density at constant entropy then provides a prediction of the temperature of the core in the initial and final stages. Since neutrinos are primarily emitted from the high-density region by neutral- and charged-current reactions, the temperature of the core plays an important role in determining their spectra [94]. At low temperatures both the density of states and entropy are expected to be proportional to the nucleon effective mass M^*

$$N(0) = \sum_t \frac{M_t^* k_{f_t}}{\pi^2},$$

$$S/V = \sum_t \frac{M_t^* k_{f_t}}{3} T. \quad (16)$$

For the same entropy per baryon, a smaller effective mass at a given density therefore translates to a higher temperature.

In Fig. 14 we depict the Skyrme, RMF and chiral isentropic lines for pure neutron matter and isospin-symmetric matter for densities up to $4\rho_0$. We use the exact expression for entropy from Eq. 12 in this plot. For low-density neutron matter ($\rho < \rho_0/2$), the Ska35s20-1.0 Skyrme interaction gives results that are consistent with the n3lo414 chiral potential, which from Fermi liquid theory [95] predicts an effective mass $M^*/M \sim 1$. Beyond nuclear matter saturation density, the differences

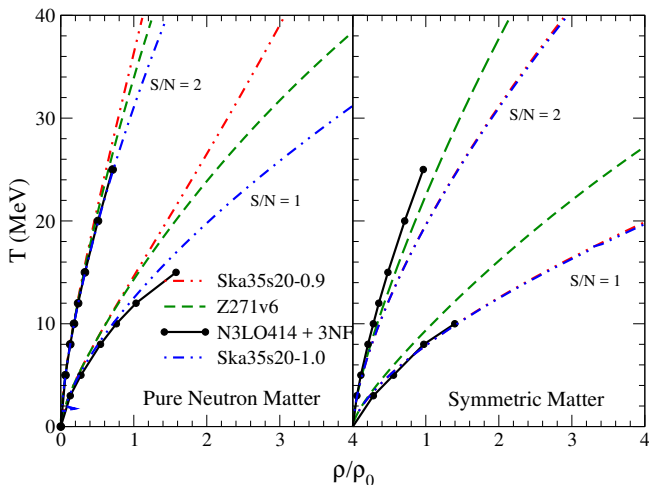


FIG. 14. (color online) Temperature versus density isentropic lines for PNM and SNM.

between the temperature of neutron matter at $S/N = 1$ can vary by up to 8 MeV for the chiral and mean field theory equations of state, while for $S/N = 2$ all models are nearly consistent. In the case of symmetric nuclear matter the two Skyrme parametrizations considered have very similar effective masses (see Fig. 12) and therefore the isentropic curves are nearly identical. At the highest temperatures ($T \gtrsim 20$ MeV) there are large variations in the predicted densities. In the microscopic calculation with the chiral n3lo414 potential, one may interpret this as a significant reduction of the effective mass at finite temperature due to a damping of collective modes [96], which normally lead to an enhanced effective mass. In general for temperatures less than $T = 10$ MeV the chiral isentropic curves are in good agreement with those from the Ska35s20-1.0 Skyrme interaction.

IV. NEUTRON STAR MASS-RADIUS RELATIONSHIP

An important feature of the ‘strong’ physics of neutron stars is the interdependence of mass and radius, which is uniquely determined by the EoS and the self-gravity of these compact objects. A relatively stiff EoS at high densities is required to generate a maximal mass of $2M_{\odot}$, which is currently the highest mass of an observed neutron star [5]. However, chiral interactions have a momentum cutoff that is comparable to the fermi momentum at about $2\rho_0$ in neutron matter, and central densities in neutron stars can reach values of $5\rho_0$ or higher. The mean field models considered in the present work can therefore be used to probe the very high density regime inaccessible to chiral effective field theory with coarse-resolution potentials. In our analysis we choose to use the chiral interaction up to the limit of its validity without model-dependent extensions. RMF models by construction remain causal, but Skyrme models can become superlu-

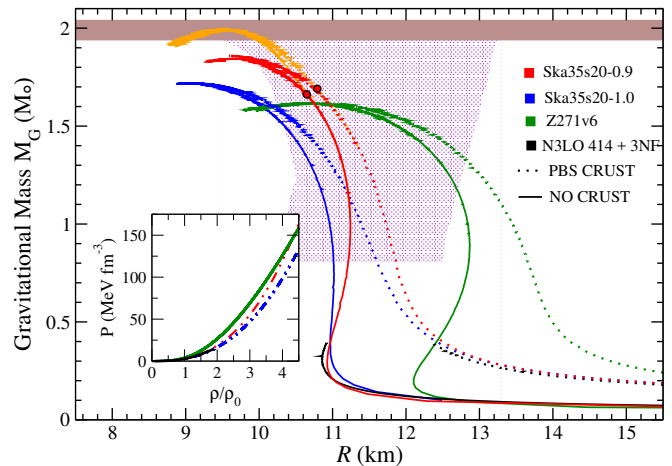


FIG. 15. (color online) Neutron star mass as a function of radius. The mass-radius observational constraint comes from Ref. [98] and the maximum neutron star mass comes from Refs. [4, 5]. We use the BPS crust EoS [99] at low densities. The solid dots indicate the transition region to the constant speed of sound equation of state.

minimal at very large densities. In the present analysis, however, we find no evidence for this behavior.

In Fig. 15 we plot the neutron star mass vs. radius in the absence of protons and light leptons at $T = 0$ from the mean field models consistent with the chiral n3lo414 equation of state at low to moderate densities. Recently, in Ref. [97] a similar analysis has been performed for relativistic mean field models consistent with the infinite matter constraints considered in Section III. Given the low values of the proton fraction found for β -equilibrated matter, this approximation is expected to be very good. We show also in Fig. 15 the current observational constraints on the mass and radius [98]. For each mean field model, we plot the mass vs. radius relationship both with and without the inclusion of the PBS crust equation of state [99].

Skyrme models employed in our work are softer at lower densities and stiffer at higher densities, compared to the relativistic mean field model Z271v6. This results in generally smaller radii at a given mass for the Skyrme interactions and a larger maximum mass. For neutron star masses greater than about $1.3M_{\odot}$, all equations of state give mass-radius relations consistent with the empirical constraints from Ref. [98]. The inclusion of a crust increases the radius by about 0.5 km for a $1.4 M_{\odot}$ neutron star and for the most massive neutron stars has a relatively small impact. This is, perhaps, a first indication that the crust equation of state used should be consistent with the underlying microphysics model given its impact in the size of typical neutron stars (of mass $1.4 M_{\odot}$). This and other implications of the crust EoS are current subject of investigation to be published in future works.

We see that none of the models employed reaches the maximal mass value of 2 solar masses, indicating that the

phenomenological interactions must be supplemented by a stiffer EoS at high densities. We identify the density above which the equation of state must be modified by employing the constant speed of sound parametrization [100] at the superluminal boundary. As a representative example, the Ska35s20.09 Skyrme interaction can generate a 2 solar-mass neutron star if the equation of state beyond $\rho = 4.5\rho_0$ is taken to be that of a liquid with constant speed of sound equal to the speed of light. The presence of the crust has only a very small effect, increasing the transition density to $\rho = 4.6\rho_0$.

However, for the high densities required for 2 solar mass neutron stars there are no other constraints on the properties of baryonic matter and our criteria is valid only for low densities. Thus, we would only like to emphasize that it is feasible to reach the mass limit by modifications of the high density regime, but the proper study of matter in this range is beyond the scope of this work.

V. CONCLUSION

We have studied the use of mean field models to reproduce zero- and finite-temperature nuclear equations of state derived from microscopic many-body theory with realistic chiral two- and three-body forces. Comparing to quantum Monte Carlo simulations employing two-body forces alone, we find that the zero-temperature neutron matter equation of state is well converged in perturbation theory up to half saturation density, with uncertainties on the order of a few percent. From this density regime we select mean field models consistent with the predictions from chiral effective field theory as well as the available empirical infinite matter constraints. We then explore consistency with chiral nuclear thermodynamics and find that the free energy as a function of the temperature for mean field models are strongly correlated with the nucleon effective mass, with smaller values giving rise to larger kinetic energy contributions and smaller entropy contributions to the free energy.

In addition we studied the effects of the single-particle dispersion relation on select astrophysical phenomena, such as neutrino absorption in the proto-neutron star neutrinosphere and the adiabatic evolution of core collapse. While the single-particle energy shift is most relevant for determining the charged-current weak reaction rates, the nucleon effective mass largely governs the isentropic temperature-density relation. For the latter quantity, significant variations are observed in the neutron matter low-entropy regime. At the largest densities considered ($\rho \sim 1.6\rho_0$), the temperature can vary by up to 50% for matter with an entropy per baryon of $S/N = 1$.

Finally, the mean field models consistent with the low-density chiral n3lo414 equation of state were used to explore the high-density regime relevant for cold neutron star matter where chiral effective field theory is expected to break down. While the mass-radius curves are consistent with present observational constraints around

$M \sim 1.5M_\odot$, all maximum neutron star masses lie below $M \sim 2M_\odot$ and the constant speed of sound parametrization was used to complete the mean field models in the high-density regime above $\rho = 4.5\rho_0$.

The present work lays the foundation for future efforts to construct consistent equations of state and neutrino response functions that are compatible with chiral effective field theory for use in numerical simulations of core-collapse supernovae and binary neutron star mergers.

ACKNOWLEDGMENTS

We thank A. Bulgac and S. Reddy for useful discussions, A. Brown for sharing the parameters of the Skyrme models used in this work, and C. Wellenhofer for providing us with the temperature- and density-dependent entropy from chiral nuclear forces. The work of J. W. Holt was supported by US DOE Grant No. DE-FG02-97ER41014. The work of A. Roggero was supported by NSF Grant No. AST-1333607. The work of E. Rrapaj was supported by US DOE Grant No. de-sc0008489. Some of the most intensive computations have been performed at NERSC thank to a Startup allocation.

VI. APPENDIX

A. Sign Problem

As explained in Section II A the main systematic bias in the CIMC calculations come from imposing a fixed-node approximation in order to deal with the sign problem. In this section we discuss additional details and estimate the impact of this approximation. First we recall that within the fixed-node approach one defines a family of *sign-problem-free* hamiltonians H_γ (see e.g., Ref. [101]). If we introduce the sign function

$$\mathfrak{s}(\mathbf{m}, \mathbf{n}) = \text{sign} \left(\frac{\langle \Phi_G | \mathbf{m} \rangle}{\langle \mathbf{n} | \Phi_G \rangle} \langle \mathbf{m} | H | \mathbf{n} \rangle \right), \quad (17)$$

where Φ_G is the wavefunction used for the fixed node procedure, we can define the off diagonal matrix elements ($\mathbf{n} \neq \mathbf{m}$) of the sign-problem-free Hamiltonian H_γ as:

$$\langle \mathbf{m} | \mathcal{H}_\gamma | \mathbf{n} \rangle = \begin{cases} -\gamma \frac{\langle \Phi_G | \mathbf{m} \rangle}{\langle \mathbf{n} | \Phi_G \rangle} \langle \mathbf{m} | H | \mathbf{n} \rangle & \mathfrak{s}(\mathbf{m}, \mathbf{n}) > 0 \\ \frac{\langle \Phi_G | \mathbf{m} \rangle}{\langle \mathbf{n} | \Phi_G \rangle} \langle \mathbf{m} | H | \mathbf{n} \rangle & \text{otherwise} \end{cases}, \quad (18)$$

while the diagonal elements are:

$$\langle \mathbf{n} | \mathcal{H}_\gamma | \mathbf{n} \rangle = \langle \mathbf{n} | H | \mathbf{n} \rangle + (1 + \gamma) \sum_{\substack{\mathbf{n} \neq \mathbf{m} \\ \mathfrak{s}(\mathbf{m}, \mathbf{n}) > 0}} \frac{\langle \Phi_G | \mathbf{m} \rangle}{\langle \mathbf{n} | \Phi_G \rangle} \langle \mathbf{m} | H | \mathbf{n} \rangle \quad (19)$$

It can be easily seen that for $\gamma = -1$ the original Hamiltonian is recovered. Furthermore if we label with E_γ

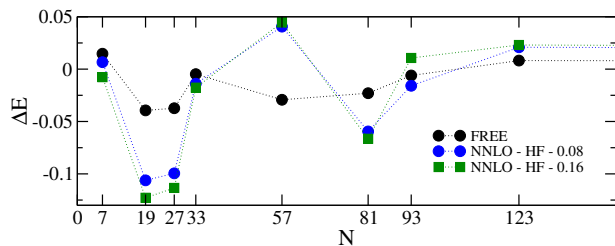


FIG. 16. (color online) Finite-size errors in the energy per particle as a function of the number of particles per spin-isospin species. The results shown are for a free gas as well as for Hartree-Fock calculations with the NNLO_{opt} interaction at the two densities $\rho = \rho_0$ and $0.5\rho_0$.

the lowest eigenvalue of a given H_γ one can prove that any linear extrapolation from two values E_{γ_1} and E_{γ_2} at $\gamma_1, \gamma_2 \geq 0$ to $E_{-1}^{\gamma_1, \gamma_2}$ provides an upper bound on the true ground state energy E_{-1} .

In the calculations presented here this procedure has been adopted by performing linear extrapolations using values at $\gamma = 0$ and $\gamma = 1$. The variation between the eigenvalues at different γ , including the extrapolated value at $\gamma = -1$ can be used as lower bounds on the missing energy contribution coming from the fixed-node approximation. We find that this spread in the case of PNM is within the estimated error bars coming from statistical uncertainties and are usually less than 20 keV per particle. In the case of SNM, however, the values at different gamma are outside the statistical error bars for densities below $0.1 - 0.14 \text{ fm}^{-3}$ but still of the order of 100 keV per particle even at the lowest densities.

This lower bound on the fixed-node error would be a good estimate provided there are no relevant contributions beyond the linear one in the γ extrapolation, a condition that cannot be checked in practice. In order to have another quantitative estimate of the systematic bias introduced by using the fixed-node approximation, we can check the sensitivity to changes in the underlying guiding wavefunction. This is analogous to the error estimates in MBPT obtained by changing the single-particle spectrum. The guiding wavefunction used in our calculations comes from the coupled-cluster double approximation with amplitudes obtained from second-order MBPT (see Ref. [55] for additional details) which clearly has zero overlap with states composed of an odd number of particle-hole excitations. In order to check the sensitivity to this choice we can set a lower bound on the overlaps of this wavefunction to any state in the Hilbert space generated by the single-particle space we have chosen. In this way we are including effectively a crude ansatz for triple and higher cluster excitations in this wavefunction that we will call CCD^* .

The effect of using this as a guiding wavefunction in the case of PNM in the density range explored in this work is just to raise the statistical error on the ground state energy and no difference can be seen outside the

error bars, which suggests that the CCD^* wavefunction provides a worse nodal constraint (higher statistical error) but the bias introduced by neglecting triples and higher correlations is smaller or comparable to the statistical errors in the calculation. This is also compatible with the estimates from coupled-cluster calculations using perturbative triples [43]. In the case of SNM the effect of using the CCD^* wavefunction is much stronger: the statistical error is comparable to the one obtained using the bare CCD wavefunction but now the extrapolated eigenvalue E_{-1} shows considerably less binding, and this effect is stronger as the density is lowered (indicating that the origin is probably the appearance of clustering in the system). For instance, in the case of the $N^3\text{LO}$ 414 interaction we find changes of about 1 MeV at $\rho = 0.02 \text{ fm}^{-3}$ and about 0.5 MeV at $\rho = 0.08 \text{ fm}^{-3}$. Since both wavefunctions provide upper bounds on the energy, estimates are always obtained with the CCD guiding wavefunction, but we can use the CCD^* results to obtain a qualitative error band. This is the procedure we employ to produce the grey band in Fig. 5.

B. Finite Size Effects

The quantum Monte Carlo calculations presented in Section II have been carried out using finite systems containing a fixed number of particles N . In order to reach the thermodynamic limit this number has to be taken as large as possible for a given density; however due to the strong dependence (N^2 for CIMC and PT2 and N^3 for part of PT3) of the computational time on the number of particles, all the results presented so far employed $N_s = 7$ for each spin/isospin species. Here we show that this is sufficient for the low densities considered in Section II.

In order to avoid degenerate ground states we choose N_s such that all states up to a Fermi momentum k_F have been filled, and in our cubic lattice this restricts the allowed particle numbers to take on the values shown on the x -axis in Fig. 16. Among these *closed-shell* configurations the ones that preserve the cubic symmetry of the underlying lattice (corresponding to $N_s = 7, 33, \dots$) have smaller deviations from the $N_s \rightarrow \infty$ limit as can be seen from Fig. 16 and are usually selected so as to minimize finite size effects. It is remarkable that for a small system with $N_s = 7$ both the free-particle energy and the interacting Hartree-Fock energies are converged to the thermodynamic limit at the $\approx 1 - 2\%$ level, similar to the $N_s = 33$ system usually employed in similar calculations.

In the left panel of Fig. 17 we plot the energy per particle in PNM for two systems composed of either $N = 14$ or $N = 66$ neutrons interacting through the NNLO_{opt} interaction obtained both with CIMC and with different orders of MBPT. The differences are very small for all calculations apart from second-order perturbation theory (PT2), which for $N = 66$ shows a stronger density dependence above $\rho \approx 0.10 \text{ fm}^{-3}$. The situation is similar with

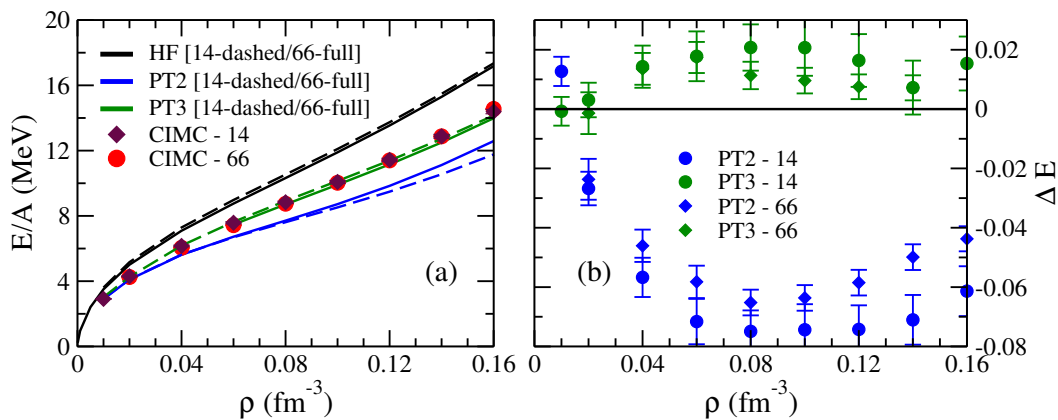


FIG. 17. (color online) (panel (a)): energy per particle in PNM computed with $N = 14$ and 66 neutrons from CIMC and MBPT using the NNLO_{opt} chiral two-nucleon potential. (panel (b)): differences between the results from CIMC and MBPT at second and third order using $N = 14$ and 66.

the other interactions used throughout this work. Since our main focus is to explore the convergence of MBPT calculations we plot in the right panel of Fig. 17 the relative difference between CIMC and both PT2 and PT3 for the case of $N = 14$ particles (black and red dots respectively) and $N = 66$ particles (green and blue dots). We see that the conclusions on the expected convergence errors are consistent for densities $\rho \lesssim 0.10 \text{ fm}^{-3}$, a density at which three-body interactions are already important. We therefore conclude that our $N_s = 7$ particle systems are large enough for our purposes in the density region where two-body interactions are the dominant contribution.

C. Effects of the Single Particle Spectrum

For all calculations presented the Hartree-Fock spectrum has been used in the single particle propagators (see e.g., Ref. [56] for details). We find that this choice yields a considerable improvement in the convergence pattern of the perturbative calculations. As can be seen from

the results in Table IV for instance, the errors at second order are approximately twice as large using a free spectrum as the ones employing self-energy corrections at the Hartree-Fock level. For nuclear matter this factor can be even larger, and it does not seem connected to the perturbativeness of the interaction as can be deduced from the increased difference in going from the harder NNLO_{opt} to the softer N^3LO 414 potential.

We conclude by pointing out that using the difference in energies obtained by varying the single-particle dispersion relation gives a qualitative understanding of the convergence of the perturbative calculations, with N^3LO 414 variations being smaller than the NNLO_{opt} ones and with a substantial increase in going from PNM to SNM. It has to be noted however that these variations cannot be used to give a quantitative estimate of the errors in the many-body calculation, which is evident from the SNM results where $\Delta(\text{PT2}_{free}-\text{PT2}_{hf})$ overestimates the error by a factor of $\approx 2 - 3$. This is however not conclusive since in SNM the CIMC calculation is not fully under control. In PNM where the difference with CIMC is a more reliable check of convergence, the errors are consistently underestimated by employing $\Delta(\text{PT2}_{free}-\text{PT2}_{hf})$.

-
- [1] J. M. Lattimer and M. Prakash, *Science* **304**, 536 (2004).
[2] A. W. Steiner, J. M. Lattimer, and E. F. Brown, *Astrophys. J.* **765**, L5 (2013).
[3] F. Özel, *Rept. Prog. Phys.* **76**, 016901 (2013).
[4] P. B. Demorest, T. Pennucci, S. M. Ransom, M. S. E. Roberts, and J. W. T. Hessels, *Nature* **467**, 1081 (2010).
[5] J. Antoniadis *et al.*, *Science* **340**, 6131 (2013).
[6] P. Danielewicz, R. Lacey, and W. Lynch, *Science* **298**, 1592 (2002).
[7] M. Dutra, O. Lourenço, J. S. Sá Martins, A. Delfino, J. R. Stone, and P. D. Stevenson, *Phys. Rev. C* **85**, 035201 (2012).
[8] K. Hebeler, J. M. Lattimer, C. J. Pethick, and A. Schwenk, *Phys. Rev. Lett.* **105**, 161102 (2010).
[9] S. Gandolfi, J. Carlson, and S. Reddy, *Phys. Rev. C* **85**, 032801 (2012).
[10] T. Krüger, I. Tews, K. Hebeler, and A. Schwenk, *Phys. Rev. C* **88**, 025802 (2013).
[11] A. Roggero, A. Mukherjee, and F. Pederiva, *Phys. Rev. Lett.* **112**, 221103 (2014).
[12] G. Włazłowski, J. W. Holt, S. Moroz, A. Bulgac, and K. Roche, *Phys. Rev. Lett.* **113**, 182503 (2014).
[13] I. Tews, S. Gandolfi, A. Gezerlis, and A. Schwenk, arXiv:1507.05561 (2015).

PNM	NNLO _{opt}			N ³ LO-414		
ρ (fm^{-3})	$\Delta PT2_{free}$	$\Delta PT2_{hf}$	$\Delta(PT2_{free}-PT2_{hf})$	$\Delta PT2_{free}$	$\Delta PT2_{hf}$	$\Delta(PT2_{free}-PT2_{hf})$
0.02	-0.0422(55)	-0.0268(56)	-0.015449(90)	-0.0239(46)	-0.0131(47)	-0.010774(51)
0.04	-0.0863(64)	-0.0567(66)	-0.02961(21)	-0.0408(48)	-0.0253(48)	-0.015511(77)
0.06	-0.1175(73)	-0.0716(76)	-0.04590(38)	-0.0473(51)	-0.0287(52)	-0.018634(99)
0.08	-0.1381(71)	-0.0749(71)	-0.06320(48)	-0.0490(52)	-0.0282(54)	-0.02079(11)

SNM	NNLO _{opt}			N ³ LO-414		
ρ (fm^{-3})	$\Delta PT2_{free}$	$\Delta PT2_{hf}$	$\Delta(PT2_{free}-PT2_{hf})$	$\Delta PT2_{free}$	$\Delta PT2_{hf}$	$\Delta(PT2_{free}-PT2_{hf})$
0.04	0.1711(15)	0.0217(13)	0.14940(19)	0.166(12)	0.040(11)	0.1264(14)
0.06	0.2829(12)	0.0946(10)	0.18832(17)	0.1965(67)	0.0540(59)	0.14250(80)
0.08	0.31699(81)	0.10439(68)	0.21260(13)	0.2185(81)	0.0662(71)	0.1523(10)

TABLE IV. Deviations from CIMC energies of 2nd order MBPT calculations for both PNM (top part) and SNM (bottom part) for two of the interactions used in this work. $\Delta PT2_{free}$ is the relative difference with respect to MBPT2 with a free spectrum in the propagators, $\Delta PT2_{hf}$ instead uses a Hartree-Fock dispersion while $\Delta(PT2_{free}-PT2_{hf})$ simply states the variation coming from changes in the single-particle spectrum. Errors in parenthesis are statistical errors coming from the CIMC result.

- [14] J. Lattimer and D. Swesty, Nucl. Phys. **A535**, 331 (1991).
- [15] H. Shen, H. Toki, K. Oyamatsu, and K. Sumiyoshi, Nucl. Phys. **A637**, 435 (1998).
- [16] M. Hempel, T. Fischer, J. Schaffner-Bielich, and M. Liebendorfer, Astrophys. J. **748**, 70 (2012).
- [17] S. Aoki, Prog. Part. Nucl. Phys. **66**, 687 (2011).
- [18] S. Aoki, Eur. Phys. J. A **49**, 81 (2013).
- [19] M. J. Savage, Prog. Part. Nucl. Phys. **67**, 140 (2012).
- [20] T. Inoue, S. Aoki, T. Doi, T. Hatsuda, Y. Ikeda, N. Ishii, K. Murano, H. Nemura, and K. Sasaki, Phys. Rev. Lett. **111**, 112503 (2013).
- [21] S. Weinberg, Physica A **96**, 327 (1979).
- [22] D. R. Entem and R. Machleidt, Phys. Rev. C **68**, 041001 (2003).
- [23] E. Epelbaum, H.-W. Hammer, and U.-G. Meissner, Rev. Mod. Phys. **81**, 1773 (2009).
- [24] R. Machleidt and D. R. Entem, Phys. Rept. **503**, 1 (2011).
- [25] N. Kalantar-Nayestanaki, E. Epelbaum, J. G. Messchendorp, and A. Nogga, Rep. Prog. Phys. **75**, 016301 (2012).
- [26] B. R. Barrett, P. Navrátil, and J. P. Vary, Prog. Part. Nucl. Phys. **69**, 131 (2013).
- [27] R. Roth, J. Langhammer, A. Calci, S. Binder, and P. Navrátil, Phys. Rev. Lett. **107**, 072501 (2011).
- [28] H. Hergert, S. K. Bogner, S. Binder, A. Calci, J. Langhammer, R. Roth, and A. Schwenk, Phys. Rev. C **87**, 034307 (2013).
- [29] E. Epelbaum, H. Krebs, D. Lee, and U.-G. Meißner, Phys. Rev. Lett. **104**, 142501 (2010).
- [30] G. Hagen, M. Hjorth-Jensen, G. R. Jansen, R. Machleidt, and T. Papenbrock, Phys. Rev. Lett. **109**, 032502 (2012).
- [31] T. Otsuka, T. Suzuki, J. D. Holt, A. Schwenk, and Y. Akaishi, Phys. Rev. Lett. **105**, 032501 (2010).
- [32] J. D. Holt, T. Otsuka, A. Schwenk, and T. Suzuki, J. Phys. G **39**, 085111 (2012).
- [33] V. Somà, C. Barbieri, and T. Duguet, Phys. Rev. C **87**, 011303 (2013).
- [34] F. Wienholtz, D. Beck, K. Blaum, C. Borgmann, M. Breitenfeldt, R. Cakirli, S. George, F. Herfurth, J. Holt, M. Kowalska, *et al.*, Nature **498**, 346 (2013).
- [35] A. Ekström, G. R. Jansen, K. A. Wendt, G. Hagen, T. Papenbrock, B. D. Carlsson, C. Forssén, M. Hjorth-Jensen, P. Navrátil, and W. Nazarewicz, Phys. Rev. C **91**, 051301 (2015).
- [36] N. Kaiser, S. Fritsch, and W. Weise, Nucl. Phys. A **697**, 255 (2002).
- [37] J. W. Holt, N. Kaiser, and W. Weise, Nucl. Phys. **A876**, 61 (2012).
- [38] J. W. Holt, N. Kaiser, and W. Weise, Phys. Rev. C **87**, 014338 (2013).
- [39] A. Gezerlis, I. Tews, E. Epelbaum, S. Gandolfi, K. Hebeler, A. Nogga, and A. Schwenk, Phys. Rev. Lett. **111**, 032501 (2013).
- [40] L. Coraggio, J. W. Holt, N. Itaco, R. Machleidt, and F. Sammarruca, Phys. Rev. C **87**, 014322 (2013).
- [41] I. Tews, T. Krüger, K. Hebeler, and A. Schwenk, Phys. Rev. Lett. **110**, 032504 (2013).
- [42] G. Baardsen, A. Ekström, G. Hagen, and M. Hjorth-Jensen, Phys. Rev. C **88**, 054312 (2013).
- [43] G. Hagen, T. Papenbrock, A. Ekström, K. A. Wendt, G. Baardsen, S. Gandolfi, M. Hjorth-Jensen, and C. J. Horowitz, Phys. Rev. C **89**, 014319 (2014).
- [44] A. Roggero, A. Mukherjee, and F. Pederiva, arXiv:1406.1631 (2014).
- [45] L. Tolos, B. Friman, and A. Schwenk, Nucl. Phys. A **A806**, 105 (2008).
- [46] S. Fiorilla, N. Kaiser, and W. Weise, Nucl. Phys. **A880**, 65 (2012).
- [47] J. W. Holt, N. Kaiser, and W. Weise, Prog. Part. Nucl. Phys. **73**, 35 (2013).
- [48] C. Wellenhofer, J. W. Holt, N. Kaiser, and W. Weise, Phys. Rev. C **89**, 064009 (2014).
- [49] C. Wellenhofer, J. W. Holt, and N. Kaiser, Phys. Rev. C **92**, 015801 (2015).
- [50] B. A. Brown and A. Schwenk, Phys. Rev. C **89**, 011307 (2014).
- [51] D. Davesne, J. Navarro, P. Becker, R. Jodon, J. Meyer,

- and A. Pastore, Phys. Rev. C **91**, 064303 (2015).
- [52] A. Bulgac, M. M. Forbes, and S. Jin, arXiv:1506.09195 (2015).
- [53] L. Coraggio, J. W. Holt, N. Itaco, R. Machleidt, L. E. Marcucci, and F. Sammarruca, Phys. Rev. C **89**, 044321 (2014).
- [54] A. Mukherjee and Y. Alhassid, Phys. Rev. A **88**, 053622 (2013).
- [55] A. Roggero, A. Mukherjee, and F. Pederiva, Phys. Rev. B **88**, 115138 (2013).
- [56] I. Shavitt and R. J. Bartlett, *Many-Body Methods in Chemistry and Physics: MBPT and Coupled-Cluster Theory*, Cambridge Molecular Science (Cambridge University Press, 2009).
- [57] G. Booth, A. Thom, and A. Alavi, J. Chem. Phys. **131**, 054106 (2009).
- [58] F. R. Petruzielo, A. A. Holmes, H. J. Changlani, M. P. Nightingale, and C. J. Umrigar, Phys. Rev. Lett. **109**, 230201 (2012).
- [59] M. Kolodrubetz and B. K. Clark, Phys. Rev. B **86**, 075109 (2012).
- [60] A. Ekström, G. Baardsen, C. Forssén, G. Hagen, M. Hjorth-Jensen, G. R. Jansen, R. Machleidt, W. Nazarewicz, T. Papenbrock, J. Sarich, and S. M. Wild, Phys. Rev. Lett. **110**, 192502 (2013).
- [61] E. Epelbaum, H. Krebs, and U.-G. Meißner, Eur. Phys. J. A **51** (2015).
- [62] F. Sammarruca, L. Coraggio, J. W. Holt, N. Itaco, R. Machleidt, and L. Marcucci, Phys. Rev. C **91**, 054311 (2015).
- [63] F. Olver, *Asymptotics and special functions*, Computer science and applied mathematics (Academic Press, 1974).
- [64] T. Melson *et al.*, arXiv:1504.07631 (2015).
- [65] B. A. Brown, Phys. Rev. Lett. **111**, 232502 (2013).
- [66] P. Klüpfel, P.-G. Reinhard, T. J. Bürvenich, and J. A. Maruhn, Phys. Rev. C **79**, 034310 (2009).
- [67] J. Dobaczewski, W. Nazarewicz, and P.-G. Reinhard, J. Phys. G **41**, 074001 (2014).
- [68] M. Kortelainen, J. Phys. G **42**, 034021 (2015).
- [69] M. Kortelainen, T. Lesinski, J. Moré, W. Nazarewicz, J. Sarich, N. Schunck, M. V. Stoitsov, and S. Wild, Phys. Rev. C **82**, 024313 (2010).
- [70] M. Kortelainen, J. McDonnell, W. Nazarewicz, P.-G. Reinhard, J. Sarich, N. Schunck, M. V. Stoitsov, and S. M. Wild, Phys. Rev. C **85**, 024304 (2012).
- [71] M. Kortelainen, J. McDonnell, W. Nazarewicz, E. Olsen, P.-G. Reinhard, J. Sarich, N. Schunck, S. M. Wild, D. Davesne, J. Erler, and A. Pastore, Phys. Rev. C **89**, 054314 (2014).
- [72] A. W. Steiner, M. Hempel, and T. Fischer, Astrophys. J. **774**, 17 (2013).
- [73] B. G. Todd-Rutel and J. Piekarewicz, Phys. Rev. Lett. **95**, 122501 (2005); G. Shen, C. J. Horowitz, and S. Teige, Phys. Rev. C **83**, 035802 (2011).
- [74] F. J. Fattoyev, C. J. Horowitz, J. Piekarewicz, and G. Shen, Phys. Rev. C **82**, 055803 (2010).
- [75] Y. Sugahara and H. Toki, Nuclear Physics A **579**, 557 (1994).
- [76] H. Toki, D. Hirata, Y. Sugahara, K. Sumiyoshi, and I. Tanihata, Nuclear Physics A **588**, c357 (1995), proceedings of the Fifth International Symposium on Physics of Unstable Nuclei.
- [77] S. Typel, G. Röpke, T. Klähn, D. Blaschke, and H. H. Wolter, Phys. Rev. C **81**, 015803 (2010).
- [78] A. W. Steiner, M. Hempel, and T. Fischer, Astrophys. J. **774**, 17 (2013).
- [79] M. Dutra, O. Lourenço, S. S. Avancini, B. V. Carlson, A. Delfino, D. P. Menezes, C. Providência, S. Typel, and J. R. Stone, Phys. Rev. C **90**, 055203 (2014).
- [80] C. J. Horowitz and J. Piekarewicz, Phys. Rev. C **66**, 055803 (2002).
- [81] S. K. Bogner, A. Schwenk, R. J. Furnstahl, and A. Nogga, Nucl. Phys. A **763**, 59 (2005).
- [82] J. W. Holt, N. Kaiser, and W. Weise, Phys. Rev. C **79**, 054331 (2009).
- [83] J. W. Holt, N. Kaiser, and W. Weise, Phys. Rev. C **81**, 024002 (2010).
- [84] K. Hebeler and A. Schwenk, Phys. Rev. C **82**, 014314 (2010).
- [85] N. Kaiser, Eur. J. Phys. A **48**, 58 (2012).
- [86] C. Drischler, V. Somà, and A. Schwenk, Phys. Rev. C **89**, 025806 (2014).
- [87] S. Gandolfi, A. Lovato, J. Carlson, and K. E. Schmidt, Phys. Rev. C **90**, 061306 (2014).
- [88] G. Martínez-Pinedo, T. Fischer, A. Lohs, and L. Huther, Phys. Rev. Lett. **109**, 251104 (2012).
- [89] L. F. Roberts, S. Reddy, and G. Shen, Phys. Rev. C **86**, 065803 (2012).
- [90] L. F. Roberts, Astrophys. J. **755**, 126 (2012).
- [91] E. Rrapaj, J. W. Holt, A. Bartl, S. Reddy, and A. Schwenk, Phys. Rev. C **91**, 035806 (2015).
- [92] G. Martínez-Pinedo, T. Fischer, and L. Huther, J. Phys. G **41**, 044008 (2014).
- [93] A. Bartl, C. J. Pethick, and A. Schwenk, Phys. Rev. Lett. **113**, 081101 (2014).
- [94] E. O'Connor and C. D. Ott, Astrophys. J. **762**, 126 (2013).
- [95] D. Davesne, J. W. Holt, A. Pastore, and J. Navarro, Phys. Rev. C **91**, 014323 (2015).
- [96] P. Donati, P. M. Pizzochero, P. F. Bortignon, and R. A. Broglia, Phys. Rev. Lett. **72**, 2835 (1994).
- [97] M. Dutra, O. Lourenço, and D. Menezes, arXiv:1510.02060 (2015).
- [98] A. W. Steiner, J. M. Lattimer, and E. F. Brown, Astrophys. J. **765**, L5 (2013).
- [99] G. Baym, C. Pethick, and P. Sutherland, Astrophys. J. **170**, 299 (1971).
- [100] M. G. Alford, G. F. Burgio, S. Han, G. Taranto, and D. Zappalá, arXiv:1501.07902 (2015).
- [101] D. F. B. ten Haaf, H. J. M. van Bemmelen, J. M. J. van Leeuwen, W. van Saarloos, and D. M. Ceperley, Phys. Rev. B **51**, 13039 (1995).